ELSEVIER

Journal of Fluids and Structures 20 (2005) 403–423

JOURNAL OF FLUIDS AND STRUCTURES

www.elsevier.com/locate/jfs

Flow past a circular cylinder in the vicinity of a plane wall

A. Dipankar, T.K. Sengupta*

CFD Laboratory, Department of Aerospace Engineering, I.I.T. Kanpur, UP 208016, India

Received 28 June 2004; accepted 15 January 2005

Abstract

Results have been reported here for flow past a stationary cylinder in the vicinity of a solid wall. Navier–Stokes equations are solved here in stream-function/vorticity formulation using an improved overset grid method while using a very high spectral accuracy compact scheme to represent the convection process. To study the effect of changing the gap (G) between the cylinder (of diameter D) and the wall, lift and drag coefficients are obtained for (a) an intermediate gap ratio of $G/D = 0.5$ and (b) a larger gap ratio of $G/D = 1.5$. Computed results are compared with flow visualization results of Price et al. for $\mathrm{Re} = 1200$ only. This problem can be viewed as one of vortex-induced instability problem where the instability arises due to mutual interaction of the vorticity field associated with the plane wall boundary layer and the vortices that are created on the cylinder surface that are shed subsequently. Such an instability mechanism was introduced in Sengupta et al. (2003a) and the flow behaviour in the present case is explained via vorticity dynamics and the developed by-pass instability theory of Sengupta et al.

1. Introduction

Flow past a circular cylinder in the vicinity of a solid wall has been a subject of research due to its engineering and physical importance. As explained in Price et al. (2002), this flow is technologically important for laying submarine cables. The proximity of the plane wall introduces additional complications to the vortex shedding behind an isolated cylinder. Because of this complexity there still remain a few aspects of the flow that require further elucidation. When fluid flows around an isolated circular cylinder, above a critical Reynolds number, alternate vortex shedding occurs in the wake. The surface pressure changes each time a vortex is shed from the cylinder. Therefore, the cylinder is subjected to a fluctuating drag and lift in addition to the mean drag and lift. When the cylinder is located near a plane boundary, the bed proximity and the velocity gradient in the boundary layer also influence the load on the cylinder.

It is to be noted that when a cylinder is kept in the near vicinity of a plane, then the vorticity distribution of the plane boundary layer is destabilized by the vortices that are created and shed by the cylinder. This has been clearly identified in Price et al. (2002) and Lei et al. (1999) for this particular flow field. While such mutual interactions can occur at large distance due to Biot–Savart law, they can have a more subtle effect in terms of triggering an instability that was explained theoretically and experimentally in Sengupta et al. (2003a) and Lim et al. (2004). Such an instabilitys, arising out of interactions between a convecting finite-core vortex and an underlying shear layer, is important as it typifies

*Corresponding author. Tel.: +91 512 259 7945; fax: +91 512 259 7561.
E-mail address: tksen@iitk.ac.in (T.K. Sengupta).

0889-9746/$ - see front matter © 2005 Elsevier Ltd. All rights reserved.
doi:10.1016/j.jfluidstructs.2005.01.001

unsteady flow separation, by-pass transition and near-wall events in a turbulent boundary layer. These have been discussed in Sengupta et al. (2003a) and the references contained therein. This instability phenomenon has been experimentally demonstrated in Lim et al. (2004), where a coherent finite size vortex has been created by a rotating and translating circular cylinder that was allowed to move at a constant speed and height (at six to nine diameters of the cylinder) over a zero pressure-gradient shear layer. The convected vortex creates a very weak streamwise pressure gradient that destabilized the flat plate shear layer at subcritical Reynolds number. From the experimental observations in Price et al. (2002) and Lei et al. (1999) it is very apparent that the plane wall shear suffers such instabilities due to shed vortices from the stationary cylinder. One notes that an inverse interaction is also likely, where the vortex shedding process from the cylinder will be affected by the vorticity distribution on the plane wall and the image vortex system of the shed vortices. In the present research, this aspect of vorticity field interaction and the consequent instabilities will be discussed in detail, based on a new instability mechanism from the disturbance energy equation derived and explained in Sengupta et al. (2003a, c). Unlike other flow instability theories, the disturbance energy equation is derived from the Navier–Stokes equation without making any assumptions and can be used to study both linear and nonlinear instabilities of general time-dependent flows.

The effect of proximity of the plane wall on the uniform flow past a stationary cylinder has been experimentally investigated by many researchers. Experiments conducted by Bearman and Zdravkovich (1978) suggested that vortex shedding is suppressed for small G/D ratios. Additionally, when vortex shedding was suppressed, separation bubbles formed both upstream and downstream of the cylinder on the solid wall. Zdravkovich (1985, 1997) examined the drag coefficient for a broad range of Reynolds numbers from 4.8×10^4 to 3.0×10^5. The results indicated that the drag coefficient was constant when the cylinder was far outside the boundary layer. As the cylinder approached the boundary layer, the drag coefficient decreased with the ratio of gap-to-thickness of the wall boundary layer (G/δ). In a recent experiment at a moderate Reynolds number of 1200, Price et al. (2002) have shown that for small gap ratios ($G/D \leqslant 0.125$), the flow through the gap is suppressed or is extremely weak, and the separation of the plane wall boundary layer occurs both upstream and downstream of the cylinder. Although there is no regular vortex shedding, there is a periodicity associated with the outer shear-layer. They also reported that for intermediate gap ratios ($0.125 \leqslant G/D \leqslant 0.5$), the flow is very similar to that of very small gaps, except that there is now a pronounced pairing between the inner shear-layer shed from the cylinder and wall boundary layer. Gap ratios higher than this are characterized by the onset of regular vortex shedding from the cylinder. There are some restrictions in conducting accurate experiments. For example, while using the PIV technique or performing flow visualization [as reported in Price et al. (2002)], very close to wall there is always some difficulty in getting a good quality picture or data. This is one of the reasons for using a computation with an accurate method (Sengupta et al., 2003b, 2004) for understanding this flow field. Additionally, computation can provide information on physical variables such as vorticity that are usually difficult to measure. However, to get reliable computational results is also not very easy, due to the complexity of the flow domain. To generate accurate results computationally, it is necessary to have orthogonal grids near the physical boundaries where vorticity is created. For a cylinder near to a plane wall, this is possible if one uses overset(chimera) grids, as shown in Fig. 1. Fig. 1(a) shows the complete arrangement of the two overset grids that have been employed. In Fig. 1(c)the Cartesian grids employed for the plane wall problem (with the cylinder removed from the domain) is shown-marked as the subdomain Ω_1 in the figure. In this sub-grid system, in the streamwise direction uniform spacing is used while in the wall-normal direction the grid-spacing is increased in an arithmetic progression. It has been shown in Sengupta (2004) that such grids ensure grid-independent solutions. Similar grid stretching has been used for the orthogonal grid around the cylinder in the radial direction (as shown in Fig. 1(b)), while the grid lines in the azimuthal direction are distributed in an equi-angular manner. In overset grid methods, the sub-problems (as shown in Figs. 1(b) and (c)) are solved in succession with boundary informations transferred via interpolation from one subdomain to the other. A larger number of points is taken in the azimuthal direction in Fig. 1(b) to ensure a good quality interpolation at the subdomain boundaries.

In Tuncer (1997) an overset grid method has been used to compute flow past a moving airfoil using a three-point interpolation technique in creating the auxiliary conditions at the subdomain boundaries, i.e. the function values at the subdomain boundary points are obtained from three nearest neighbours belonging to the other subdomain. However, preliminary calculations for the present problem revealed that this interpolation technique is not adequate, specially for small G/D ratios. In the present work we have developed a new five-point interpolation scheme to avoid the above-mentioned problem. Furthermore, a very high accuracy scheme has been used here as given in Sengupta et al. (2003b, 2004) and Sengupta (2004) for calculating the present flow field.

A first set of results are reported here for the two cases of intermediate ($G/D = 0.5$) and large ($G/D = 1.5$) gap ratios for a moderate Reynolds number of 1200 (based on the diameter of the cylinder and the free-stream speed). This value of Reynolds number corresponds to the experimental case reported in Price et al. (2002). The main focus in the present work is to report the lift and drag experienced by the cylinder in the presence of a solid wall and compare them

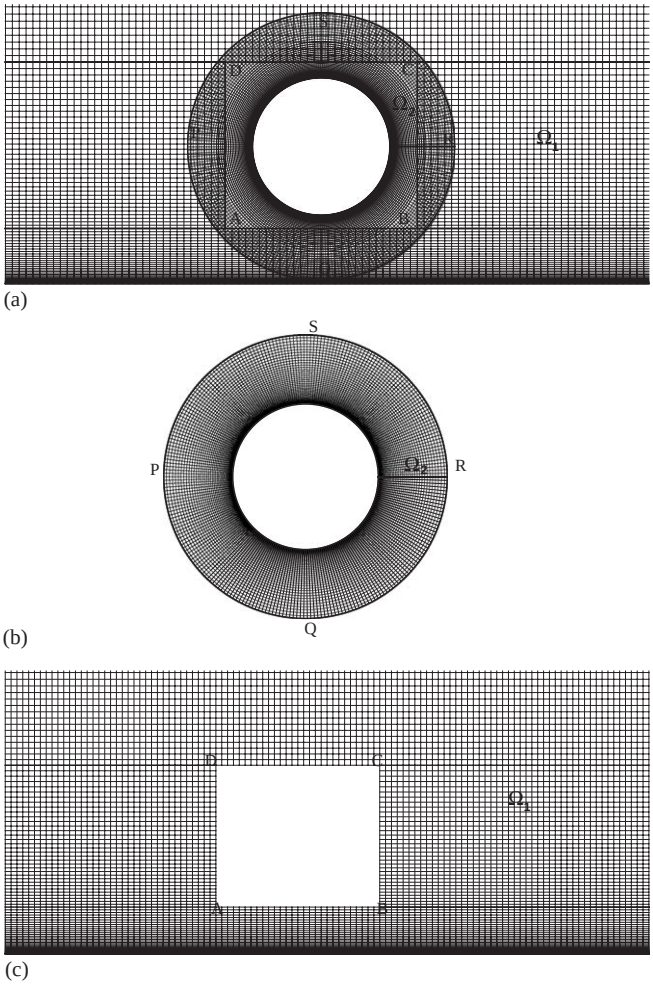

Fig. 1. The overset subgrids: (a) overall grid point distribution; (b) subgrid for cylinder; (c) parent grid for solid wall.

qualitatively with experimental results. The observed flow behaviour is then explained in terms of vorticity dynamics and an instability mechanism for unsteady flows proposed in Sengupta et al. (2003a).

The paper is structured in the following manner. In Section 2, a brief account of the governing equations and numerical methods is provided with the axillary conditions. In Section 3 we compare the computed solution with the experimental results, along with explanations for the observed flow behaviour. In Section 4, we discuss the vorticity dynamics and the vortex-induced instability. We close the paper by providing some conclusions in Section 5.

2. Governing equations and numerical methods

In the overset grid method the computational domain consists of structured sub-grids, that overlay on each other. The structured sub-grids created around each component in the flow field are put together to discretize the whole computational domain that are then computed in sequence. The Navier–Stokes equations are then solved in each subdomain independently, using an appropriate set of boundary conditions. In addition to the boundaries of the computational domain, sub-grids have inter-grid boundaries with the neighbouring donor sub-grids. In solving the problems in different subdomains therefore requires appropriate boundary conditions on these inter-grid boundaries. As discussed earlier, these boundary conditions are obtained by interpolating data from neighbouring donor sub-grids. For example, in Fig. 1(c), the conditions on the inter-grid boundary ABCD of subdomain Ω_1-that oversets on

subdomain Ω_2-is obtained from Ω_2. In a similar way, a boundary condition on inter-grid boundary PQRS is obtained from the neighbouring points of Ω_1.

Initial conditions are chosen such that we already have a fully developed laminar boundary layer over the plane wall in the absence of the cylinder—corresponding to the experimental conditions of Price et al. (2002). The boundary layer thickness at the cylinder location is $\delta = 0.44D$ [as given in Price et al. (2002)]. To achieve this, the Blasius profile over the flat plate is superimposed onto the potential flow solution of a stationary cylinder near to a plane wall. The potential flow is in turn obtained using the method of images, as given in Robertson (1969). Using this initial condition, the two-dimensional Navier–Stokes equations are solved here in stream function and vorticity formulation, which in nondimensional form is given by

$$\nabla^2\psi = -\omega, \tag{2.1}$$

$$\frac{\partial\omega}{\partial t} + \mathbf{V}\cdot\boldsymbol{\nabla}\omega = \frac{1}{\mathrm{Re}}\nabla^2\omega, \tag{2.2}$$

where ω is the out-of-plane component of vorticity defined by $\omega = (\boldsymbol{\nabla}\times\mathbf{V})\cdot\hat{\mathbf{k}}$ and the velocity is related to the stream function by $\mathbf{V} = \boldsymbol{\nabla}\times\boldsymbol{\Psi}$, where $\boldsymbol{\Psi} = (0, 0, \psi)$. This formulation avoids the problems of pressure–velocity coupling and satisfaction of mass conservation everywhere in the flow field, in contrast to the primitive variable formulation. Eqs. (2.1) and (2.2) are solved in the physical plane using the rectangular grid in the subdomain Ω_1. Working in the physical Cartesian grid allows one to avoid aliasing error problems [as shown in Sengupta (2004)] while solving Eq. (2.1). Similarly, aliasing error is absent for discretizing the physical dissipation terms of Eq. (2.2). For the circular domain, Ω_2, the flow is computed in the transformed (ξ, η)-plane where

$$x = r(\eta)\cos 2\pi\xi \quad \text{and} \quad y = r(\eta)\sin 2\pi\xi, \tag{2.3}$$

in which $0 \leqslant \xi, \eta \leqslant 1$ and

$$r(\eta) = r_0 + \frac{\eta}{\Delta\eta}\left[\Delta r_0 + \frac{d}{2}\left(\frac{\eta}{\Delta\eta} - 1\right)\right], \tag{2.4}$$

where r_0 indicates the radius of the cylinder, Δr_0 is the spacing of the first radial line and d is the increment of the successive grid line spacing. This type of grid removes alteration of convection and lowest order numerical dissipation, as shown in Nair et al. (1998) and Sengupta (2004).

The governing Poisson equation for total pressure (p_t) is obtained by taking the divergence of the Navier–Stokes equation in rotational form. This is solved here for calculating loads and pressure field in the circular domain Ω_2. For an orthogonal curvilinear co-ordinate system this is given as

$$\frac{\partial}{\partial\xi}\left(\frac{h_2}{h_1}\frac{\partial p_t}{\partial\xi}\right) + \frac{\partial}{\partial\eta}\left(\frac{h_1}{h_2}\frac{\partial p_t}{\partial\eta}\right) = \frac{\partial}{\partial\xi}(h_2 v\omega) - \frac{\partial}{\partial\eta}(h_1 u\omega), \tag{2.5}$$

where h_1 and h_2 are the scale factors given by $h_1 = (x_\xi^2 + y_\xi^2)^{1/2}$ and $h_2 = (x_\eta^2 + y_\eta^2)^{1/2}$.

The stream function equation (2.1) and the pressure Poisson equation (2.5) are solved using BI CG-STAB method of Van Der Vorst (1992). The vorticity transport equation (VTE) is solved by discretizing the diffusion term by a second-order central difference scheme and the time derivative by a four-stage Runge–Kutta scheme. The convection terms are evaluated by using the spectrally accurate compact scheme introduced in Sengupta et al. (2004).

To control aliasing and retain numerical stability an explicit fourth dissipation term $\beta h^3(\partial^4 u/\partial x^4)$ (or $(\partial^4 u/\partial\eta^4)$) is added at every point with $\beta = 0.03$. There are some excellent properties of this compact scheme in providing higher accuracy [as recorded in Sengupta et al. (2003a) and Sengupta (2004), that is not repeated here] while using fewer grid points than what would have been required with higher-order explicit scheme [as used in Sengupta et al. (2003c)]. The overall speed-up of the Navier–Stokes solver based on compact scheme is an order of magnitude over explicit higher-order-method based solvers. Freestream conditions are used at the inflow and the outer boundary of the subdomain Ω_1, as defined in Fig. 1. At the outflow, a convective boundary condition is applied to ensure smooth passage of convecting vortices. The loads acting on the cylinder are obtained by solving the pressure Poisson equation, Eq. (2.5), in subdomain, Ω_2 only. The required Neumann boundary conditions on the physical surface and in the field at PQRS are obtained from the normal (η) momentum equation given by

$$\frac{h_1}{h_2}\frac{\partial p}{\partial\eta} = -h_1 u\omega + \frac{1}{\mathrm{Re}}\frac{\partial\omega}{\partial\xi} - h_1\frac{\partial v}{\partial t}. \tag{2.6}$$

The same procedure can be applied for calculating the pressure field in the subdomain Ω_1 as well; but this has not been performed and reported here.

In time advancing the VTE (Eq. (2.2)), we have used the four-step Runge–Kutta method, whose properties have been studied, when used along with the compact schemes in Sengupta (2004). The time step chosen was 10^{-3} for the $G/D = 0.5$ case and 5×10^{-4} for the higher gap-to-diameter case.

3. Results and discussion

In this paper, computed results for $\mathrm{Re} = 1200$ only are shown and compared with the flow visualization pictures presented in Price et al. (2002). We discuss two cases separately, detailing the qualitative changes in flow behaviour as the gap-to-diameter ratio is increased from 0.5 to 1.5 for the same Reynolds number. For the subdomain Ω_1, a uniformly distributed grid has been employed with the spacing of $\Delta x = 0.05$ in the streamwise direction. In the wall-normal direction, a nonuniform mesh with 151 points have been taken for $G/D = 0.5$ case, while 192 points have been taken for the larger gap ratio case. In both cases, the first grid line is spaced at a distance of $\Delta y = 0.005$ from the wall. For the subdomain Ω_2, in the azimuthal direction 251 equi-angular points have been taken. For the $G/D = 0.5$ case, there are 43 points taken in the radial direction, while this is increased to 72 points for the larger gap ratio case. For both the cases, the first azimuthal line is placed at a distance of $\Delta r = 0.001$. The governing equations have been nondimensionalized with the diameter of the cylinder as the length scale (D) and the free-stream velocity U_∞, for the velocity scale. These two scales define the time scale as D/U_∞, so that the Reynolds number is given by $\mathrm{Re} = U_\infty D/\nu$. In all the results presented, the figures are given in terms of the nondimensional time.

In Figs. 2(a) and (c), the lift and drag coefficients for both the cases are shown as a function of time, using the standard convention of lift as positive in the upward direction and drag as negative when acting against the flow direction. The variation in lift force is associated with the movement of the front stagnation point on the cylinder. The time variation of the location of the front stagnation point for both the cases is shown in Fig. 2(d). For the smaller gap ratio case, the time average of the lift value is 0.228, and this value increases to 0.253 for the larger gap ratio case. Corresponding values for the drag coefficient are -1.135 and -1.872, respectively. The force coefficient values follow the same trend as reported in Lei et al. (1999) for the same gap ratios—but at higher Reynolds numbers. For the small gap ratio, the oncoming flow to the cylinder has nonuniform large shear and this suppresses perturbations imposed by the cylinder. The effect of shear in suppressing vortex shedding has been reported in Kiya et al. (1980). When the cylinder is moved up to $G/D = 1.5$, the flow past the cylinder will be influenced less by the plane wall shear, as compared to the previous case. This will therefore display larger variation of forces acting on the cylinder for the larger gap ratio case—as seen in Fig. 2(c). The displayed variation of the location of the front stagnation point in Fig. 2(d) shows that the front stagnation point remains above the mean line for the lower gap ratio case, while it is pushed below the mean line for the $G/D = 1.5$ case. The time-averaged location for these two cases is given by $\theta_s = 3.63^\circ$ and -3.50° for $G/D = 0.5$ and 1.5, respectively. For this unsteady flow, it is also instructive to perform frequency analysis of the force time history, particularly the lift. This will help one investigate, whether a dominant flow periodicity exists in the wake or not, apart from finding out the correctness of the computations. In Fig. 2(b), the Fourier transform of the lift coefficient is plotted as a function of frequency and the most dominant frequency marked in the figure corresponds to a Strouhal number of 0.293, which compares favourably with the data provided in Fig. 8(b) of Price et al. (2002). It must, however, be pointed out that there are other significant higher frequencies present in the time trace as well. For the higher gap ratio case, the Strouhal number reduces to a value much below that for an isolated cylinder. The enhanced unsteadiness for the latter case is due to mutual vortex-induced instability triggered by the two vorticity distributions ofthe plane wall and the shear layer of the cylinder.

Flow visualization results for $G/D = 0.5$ at $\mathrm{Re} = 1200$ in Price et al. (2002) show that the shear layers from the top and bottom surfaces curl up into an alternating sequence of vortices of differing strength. These vortices destabilize the shear layer on the plane wall downstream of the cylinder, triggering unsteady separation from the wall in the vicinity of the vortex formation region in the wake of the cylinder. This separation appears to be coupled in a periodic manner with the vortex shedding from the cylinder. This flow behaviour is confirmed by computed results shown in Figs. 3 and 4. This is explained by the streamline contour plots shown in Figs. 3(a) and (b) for the indicated time intervals for $G/D = 0.5$. In the first interval the lift and drag values come down following a flat plateau. In the second interval the lift and drag increase following another flat plateau. In Fig. 3(a) the load does not change as the vortex pair in the near-wake remains stable during $t = 8-10$, after which the top vortex is ejected out and the front stagnation point moves up causing the cylinder to experience a net downward force. During the time interval $t = 66-71$ the front stagnation point moves up as the main wake-vortex moves away, causing an increase in the lift value experienced by the cylinder. The proximity of the cylinder to the wall significantly alters the dynamics of the near- and far-wake of the cylinder. The flow separation phenomenon from the plane wall is directly determined by the induced adverse pressure gradient, both in the

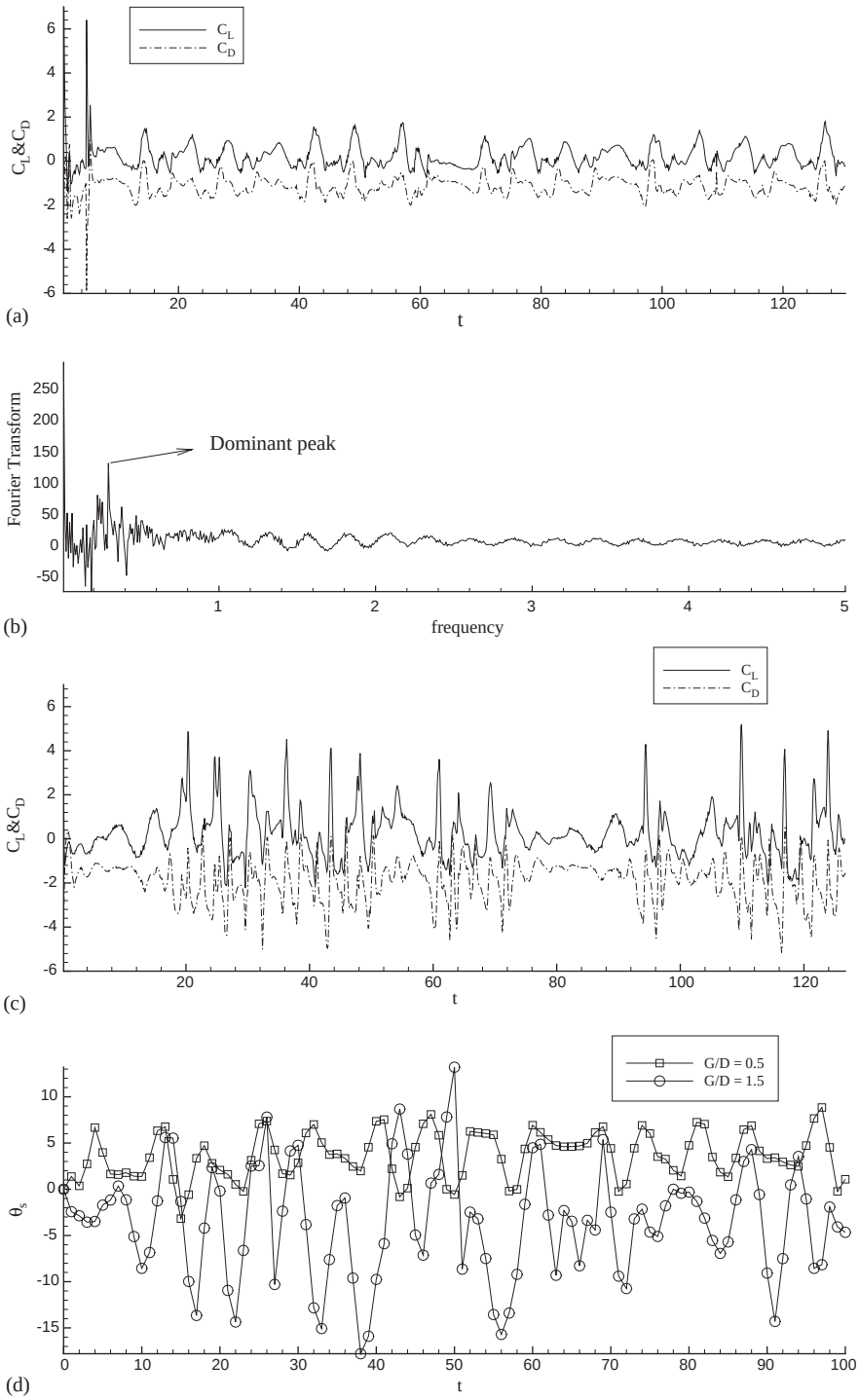

Fig. 2. Load histories for (a) $G/D = 0.5$; (b) the Fourier transform of C_L as given in (a); (c) $G/D = 1.5$ and (d) location front stagnation point for the above two cases shown as a function of time.

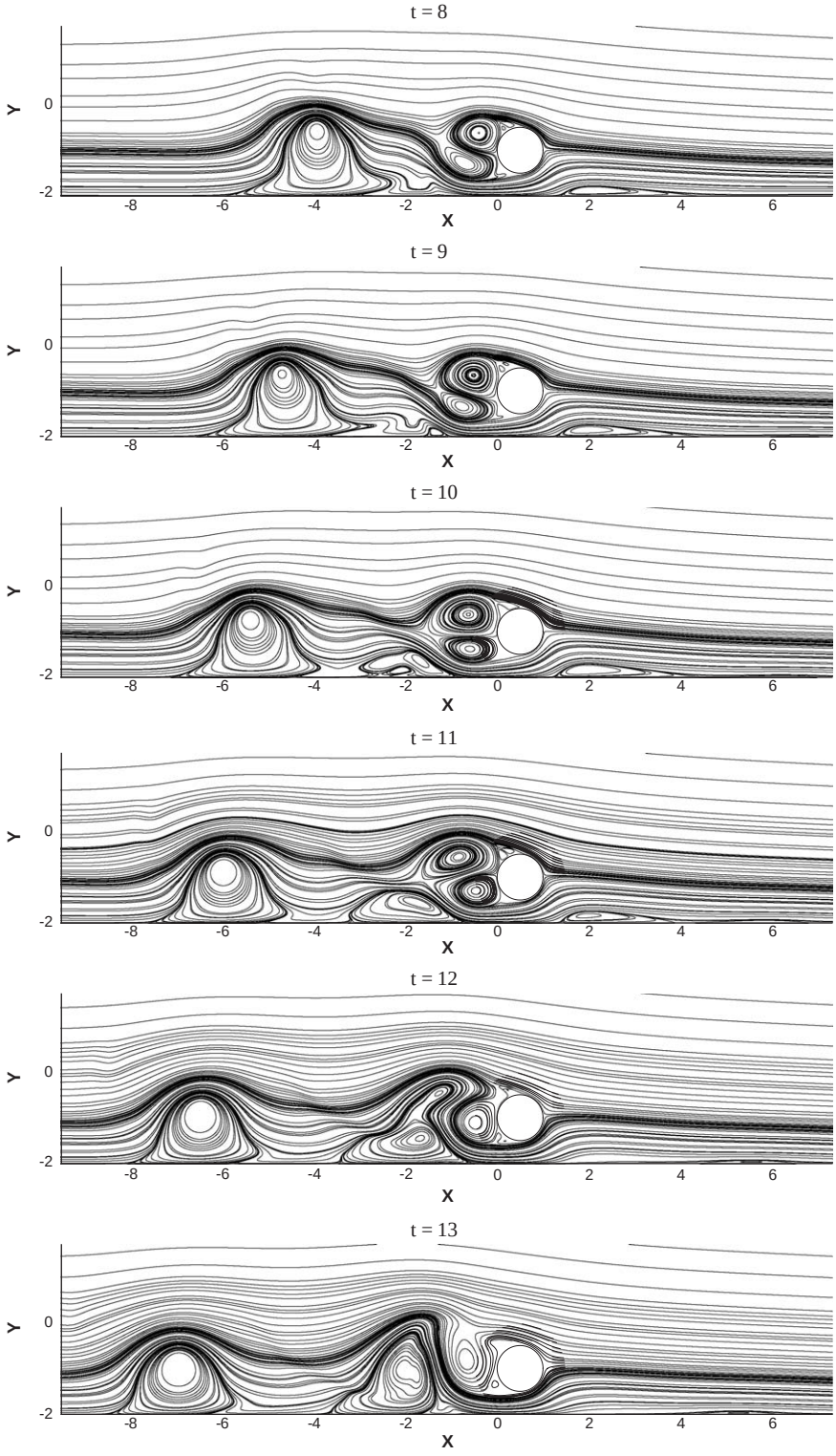

Fig. 3. Stream function contours at indicated times for (a) $G/D = 0.5$, (b) $G/D = 0.5$. (c) Comparison of experimental and computational results for the case of $\mathrm{Re} = 1200$ and $G/D = 0.5$. Shown in (i) computed vorticity contours; (ii) computed streamline contours and (iii) experimental results due to Price et al. (2002).

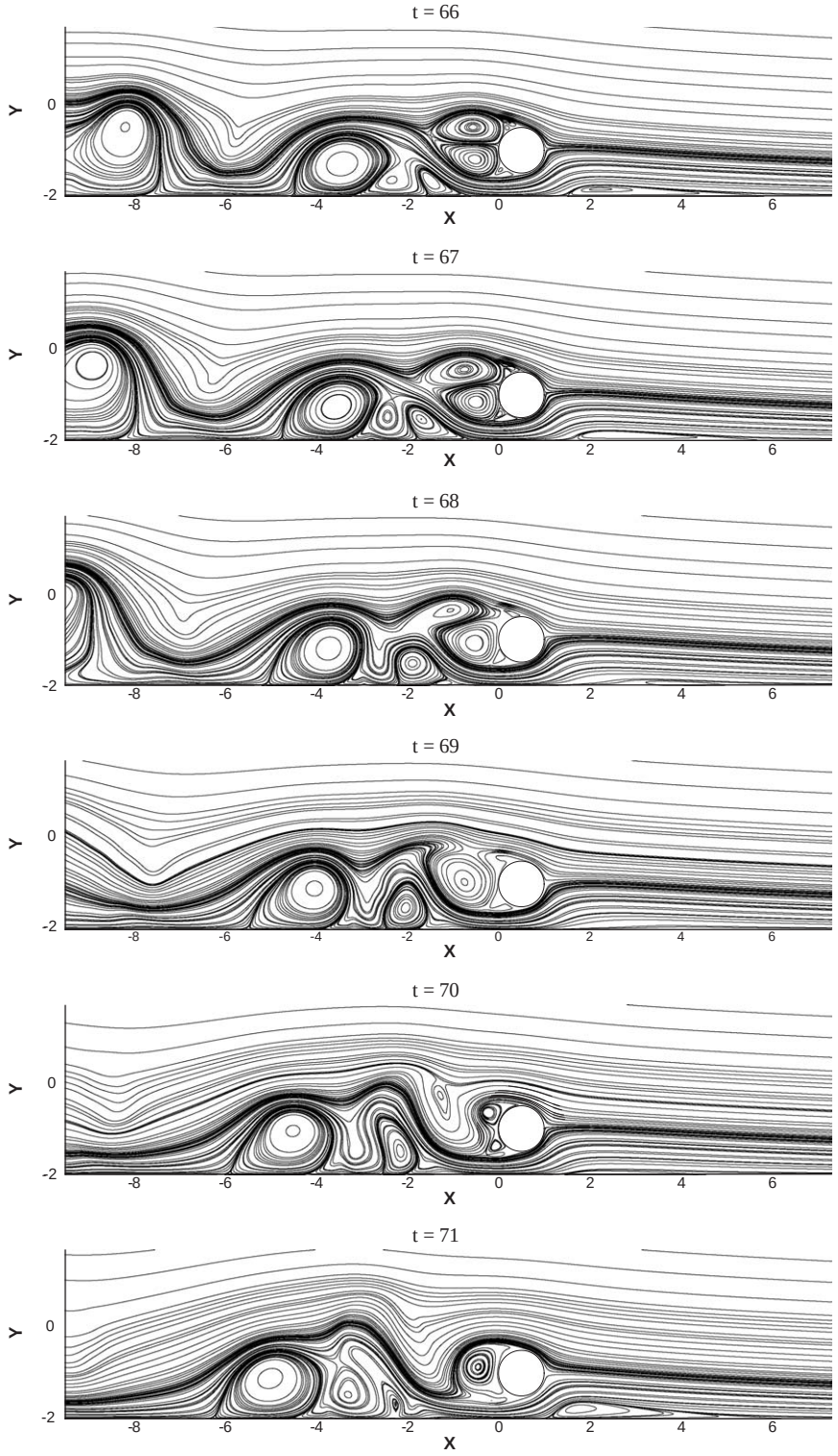

Fig. 3. (*Continued*)

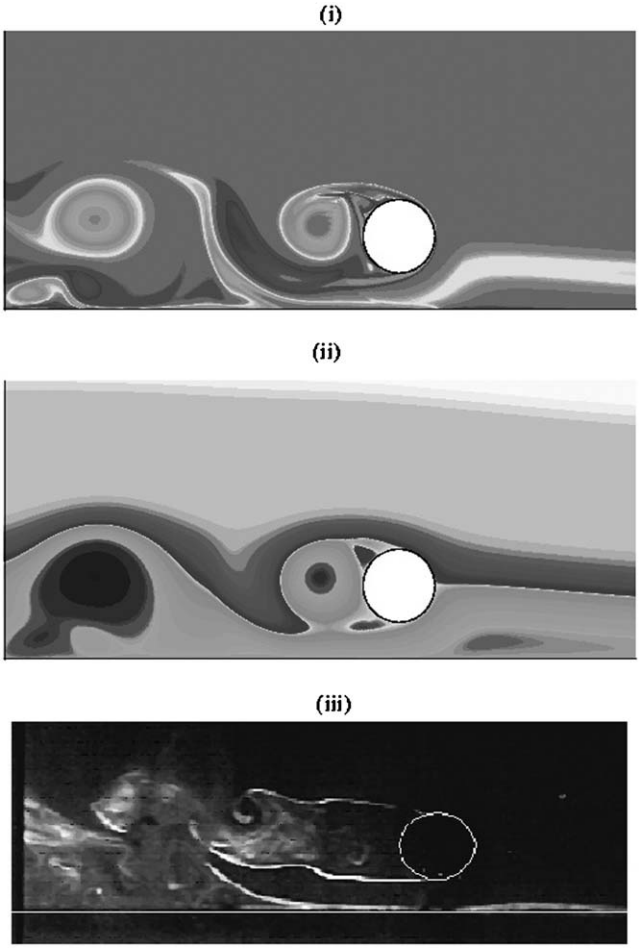

Fig. 3. (*Continued*)

up- and downstream direction of the cylinder, as explained in Sengupta et al. (2003a) and Lim et al. (2004) in terms of a vortex-induced instability. Upstream of the cylinder, on the plane wall, the plotted contours clearly indicate streamline divergence, and exactly below this one notices unsteady flow separation. Downstream of the cylinder, the presence of shed vortices produces an adverse pressure gradient that in turn causes unsteady separation of the plane wall shear layer. It is noted that the presence of shear in the oncoming flow for the $G/D = 0.5$ case delays and weakens the vortex shedding from the cylinder. The effect of shear on vortex shedding was reported by Kiya et al. (1980) and it was shown that the vortex shedding behind the cylinder was delayed up to $\mathrm{Re} = 81$ for oncoming flow with linear shear. Such effects are diminished with increased G/D.

To show the correctness of the computations presented here, in Fig. 3(c) results for $G/D = 0.5$ at $\mathrm{Re} = 1200$ are shown alongside the flow visualization figure from Price et al. (2002). In the top frame, the vorticity contours are shown, while the middle frame shows the corresponding streamline contours. For the experimental visualization figure shown in the bottom frame, the time instant is not provided and the shown computed results are at $t = 122$, noting that similar matches were also seen at $t = 107$ and 115 as well. For this case, the shear layer from the top and bottom surfaces curl up into an alternating sequence of vortices of differing strength. We would like to note that the 2-D computations show a shorter formation length of the wake structure than that is obtained in the experiment for $\mathrm{Re} = 1200$. However, the main flow features seen in the computations and experiments are identical.

For the larger gap ratio case ($G/D = 1.5$), some representative streamline contour plots are shown in Fig. 4, for $t = 40-45$. During this time interval, the lift and drag vary significantly and this is also indicated by the variation of the position of the front stagnation point in these figures. The wake dynamics once again is affected by the induced

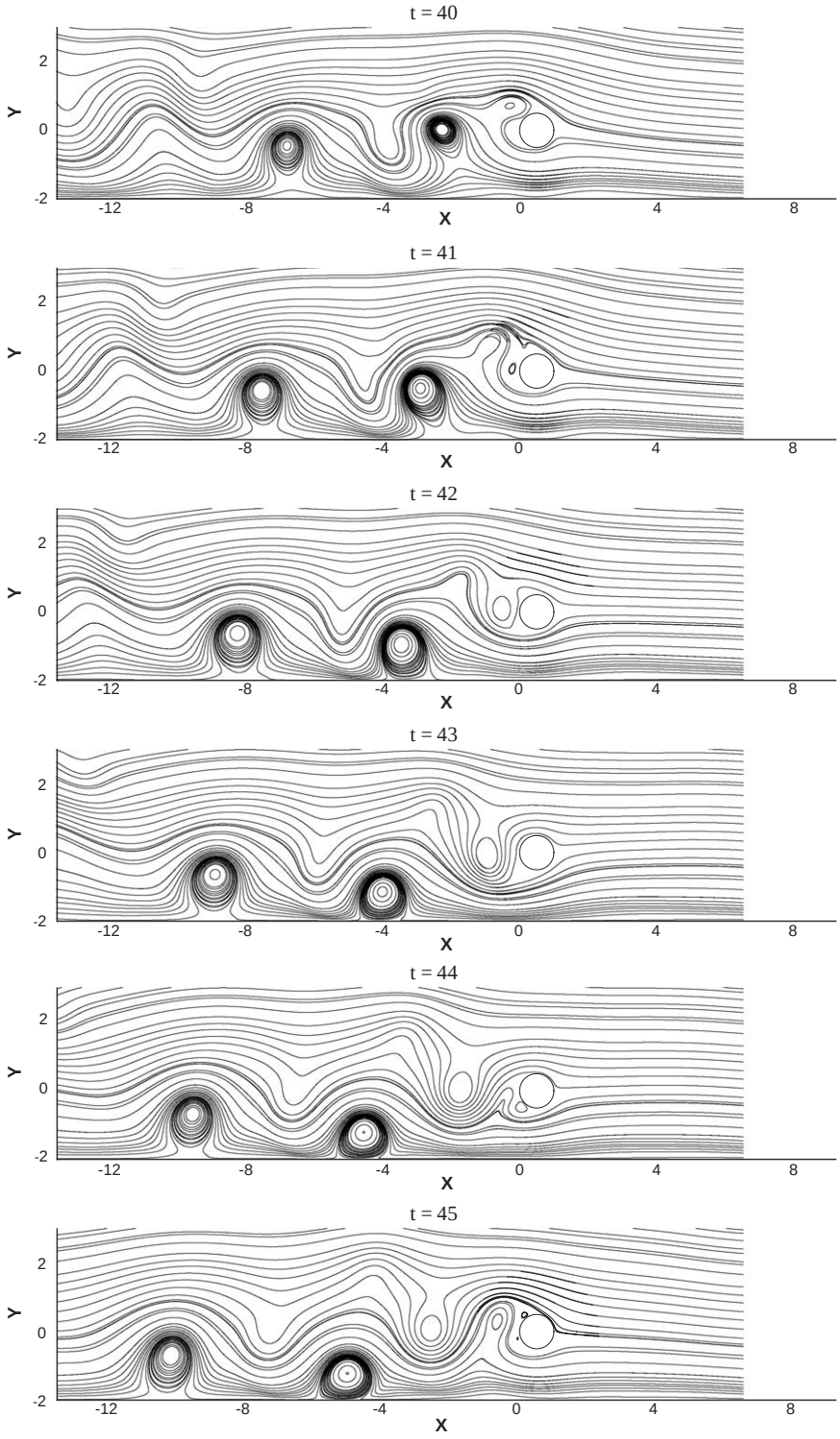

Fig. 4. Stream function contours at indicated times for $G/D = 1.5$.

unsteady separation on the downstream direction due to the vortex-induced instability-generated coherent structures on the plane wall. However, in this case the unsteady separation on the upstream side is significantly weaker in comparison to the previous case.

4. Vorticity dynamics and instability

4.1. Vorticity dynamics

Vorticity contours are shown for $G/D = 0.5$ case in Fig. 5. In the drawn contours, a positive vorticity field is shown by solid lines, while a negative vorticity is drawn by hatched lines. During this phase, the onset of asymmetry in the near-wake is pronounced and quick. The presence of the plane wall shear causes the vortex pair in the near-wake to move upward at an angle, as can be seen from the frame at $t = 9$. Also, the positive vorticity manifests itself as an elongated chain of vortices stringed together, originating from the lower half of the cylinder, as seen at $t = 12$. At the same time, another positive vorticity patch is seen to originate from the shoulder of the cylinder. Negative vorticity from the cylinder originates in between these two positive vorticity patches. Another interesting aspect of the vorticity dynamics is the way the shed positive vortex from the lower half of the cylinder anchors itself to the plane wall—labelled as A in the various time frames. At $t = 18$, the elongated positive vortex is seen above plane wall shear layer, which is seen here as a negative vorticity patch. However, due to Biot–Savart interaction the trailing part of this elongated vortex attaches itself to the plane wall in the form of a attached bubble, as can be seen at $t = 19$ and 20.

The complex vortex interaction also shows that some vortical structures move upstream. This can be seen near the outflow boundary during $t = 16-22$. Note that, at $t = 18$ a small positive vortex is seen at the outflow boundary that at subsequent times is seen to move upstream at later time. At $t = 23$, one can see a pair of such upstream propagating vortices. However, such weak vortices dissipate themselves, as they are not seen at $t = 25$.

Another interesting unit process is the interaction of two positive vortices near the wall. These vortices are marked as P_1 and P_2 in the frame at $t = 21$. These two vortices approach each other and interact strongly. Because of the presence of the negative vorticity of the plane wall shear layer, the vortex P_2 weakens and eventually disappears, as seen at $t = 25$.

The most important unit process of the vorticity dynamics for this small gap ratio case is demonstrated next, where we track the evolution of a vortex pair. These have been identified as V_1 and V_2 in the plot at $t = 40$. The vortex V_1 that stays on the outer edge of the shear layer moves much faster in the downstream direction as compared to V_2. This is evident from the frames shown at $t = 46, 49$. With time, V_2 moves close to the plane wall, and at $t = 50$ one notices the formation another small vortex, V_2'. Similar to this vortex pair, another vortex pair, identified as V_3 and V_4, can be seen at $t = 51$. Once again V_3 migrates faster, as shown at $t = 53$. By $t = 56$, it is seen that V_3 leaves the computational domain. In the computational domain, one can notice the movement of the vortices V_2, V_2' and V_4 at $t = 58, 60, 62$. At $t = 63$, V_2' is seen to leave the computational domain. The vortex V_2 is seen to weaken and disappear at $t = 69$. The vortex V_4, which has a distinct identity till $t = 67$, is seen to merge with another positive vortex and convect out of the domain at $t = 71$. This type of vortex evolution is a typical unit process for the intermediate gap ratio cases.

For the increased gap ratio case of $G/D = 1.5$, the results are displayed in Fig. 6. In this case, due to the increased gap between the cylinder and the plane wall, the imposed pressure gradient by the cylinder is lower and the flow separation on the plane wall upstream of the cylinder is very weak. Vortex-induced separation is clearly evident on the downstream side of the cylinder caused by the shed vortices and is visible right from the beginning, occurring ahead of the shed vortex. At $t = 5$ this is clearly seen, and such a recirculating bubble is seen to convect downstream with time. The other major difference of this case from the previous one is that the positive vortex is strictly shed from the lower half of the cylinder and no positive vortex patch is seen from the shoulder of the cylinder. Here also one notices the elongated positive vortex structure that tears at regular intervals (as seen between $t = 13$ and 14 and again between $t = 17$ and 18).

Here the positive vortices, even when they are not close to the wall, move at differential speeds. For example, the vortices marked as P_1 and P_2 in Fig. 6 are shown in frame at $t = 22$. As P_1 moves slower, the negative vortex in between is strained in the wall-normal direction. The imposed strain is so large that the negative vortex tears into two, as seen in the frame at $t = 28$, before its complete tearing at $t = 30$ (not shown here). The relatively larger spacing of the wake vortices from the plane wall causes no strong positive vortices on the latter—another distinct effect of gap ratio. Apart from vortex tearing, one can also note vortices of the same sign merging. This is shown in the frames at $t = 40, 41$ and 43, where the two vortices P_3 and P_4 are shown to coalesce.

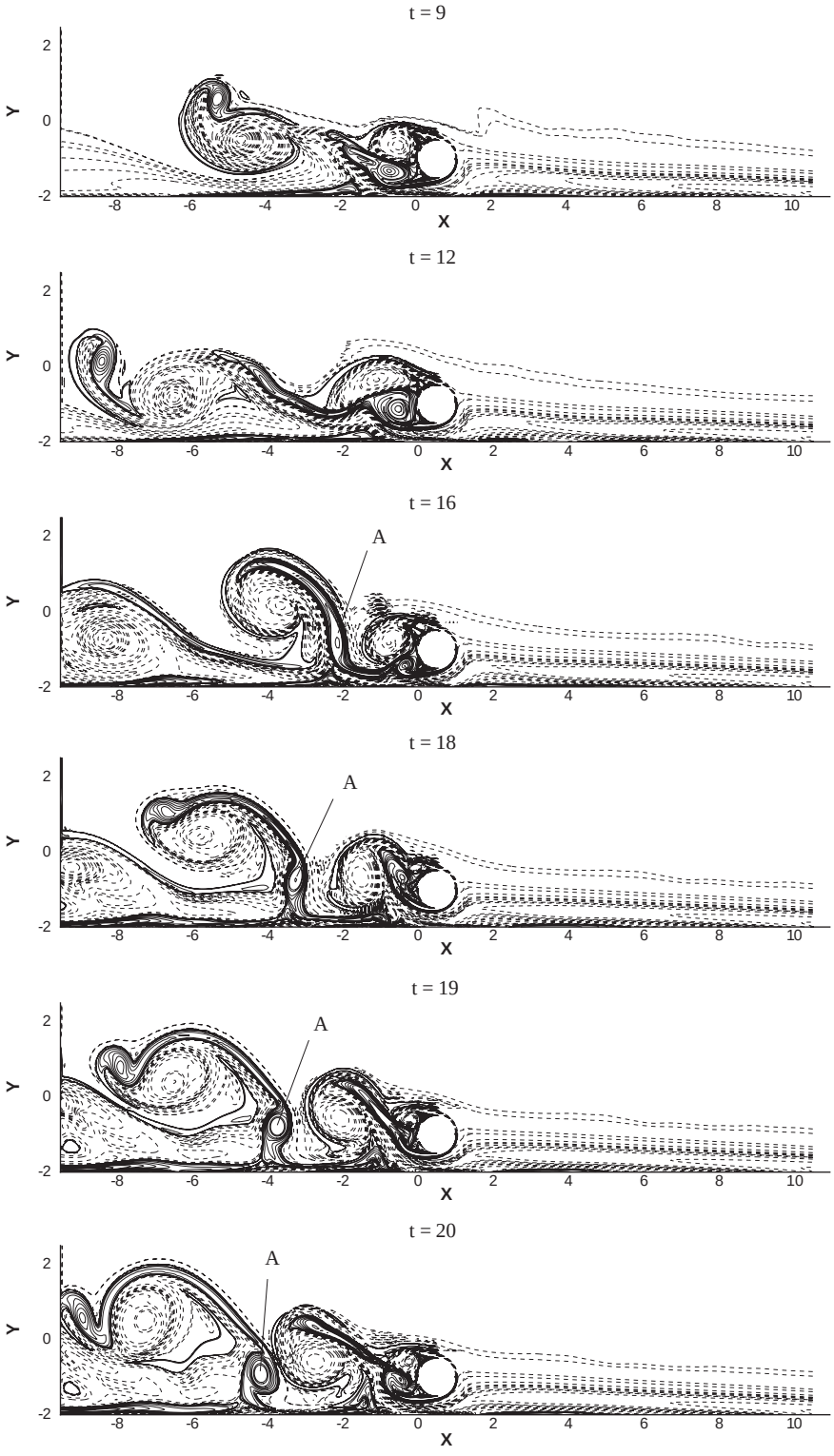

Fig. 5. Vorticity contours at indicated times for $G/D = 0.5$. The dashed lines are the negative vorticity contours.

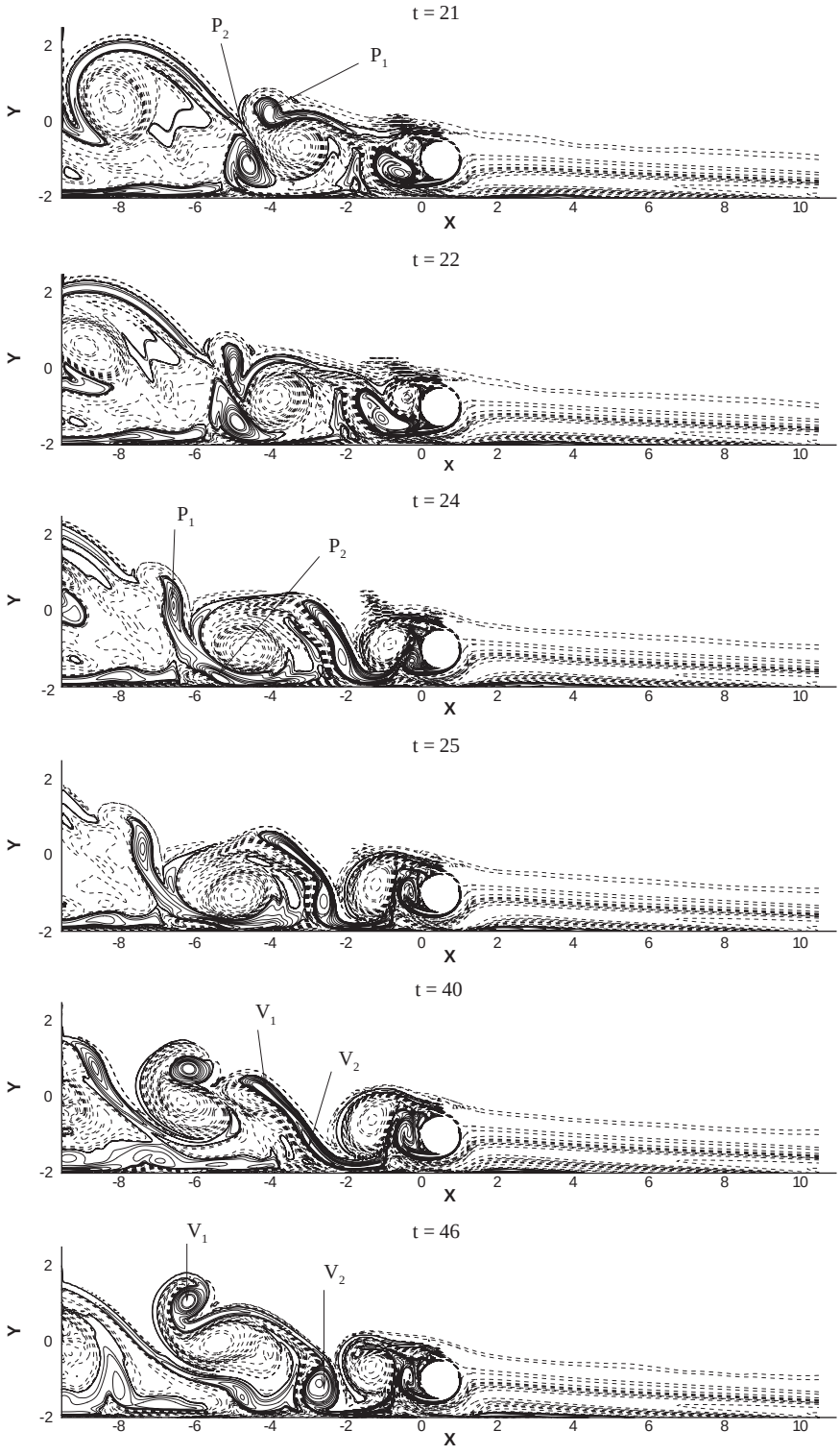

Fig. 5. (*Continued*)

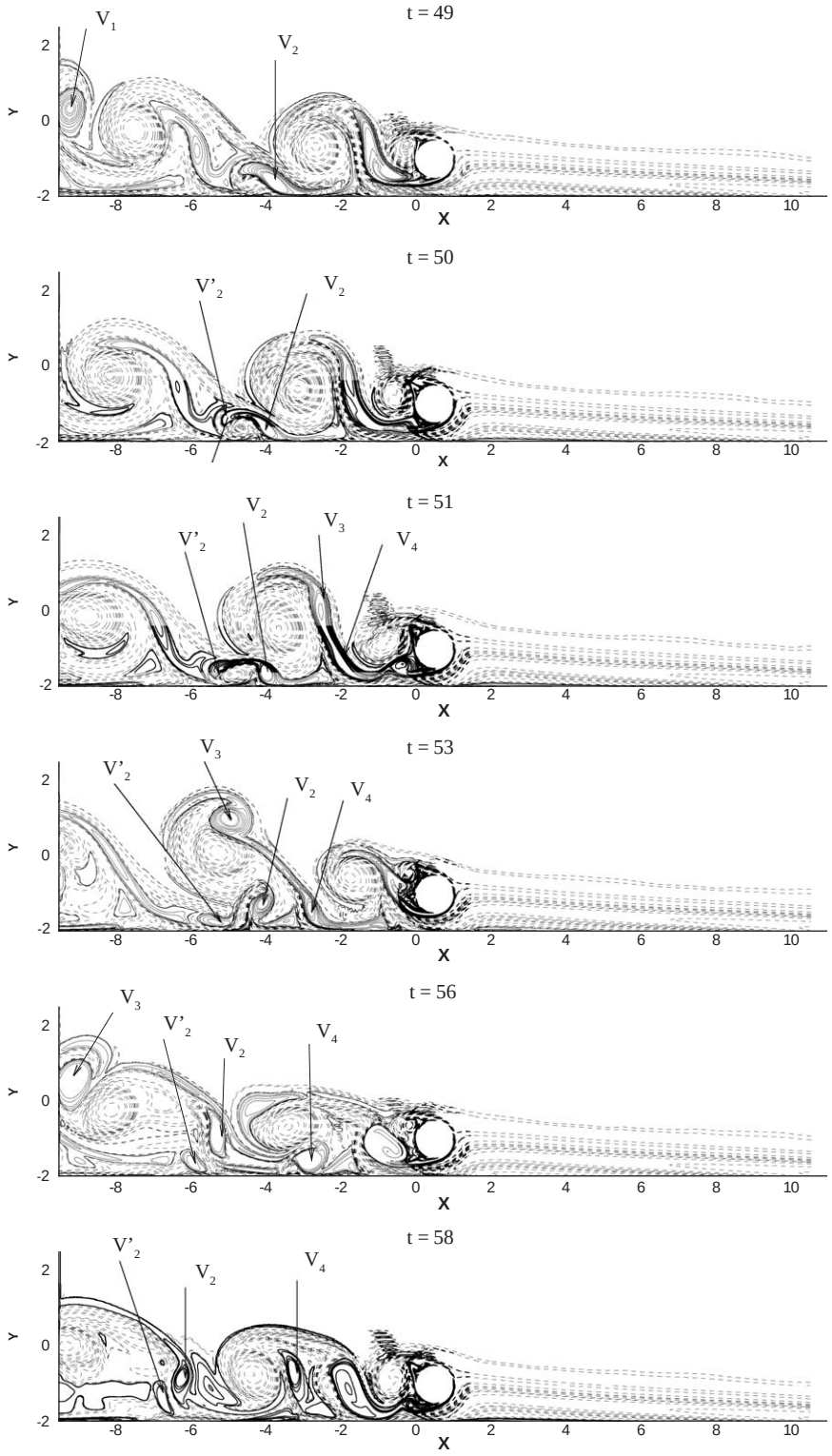

Fig. 5. (*Continued*)

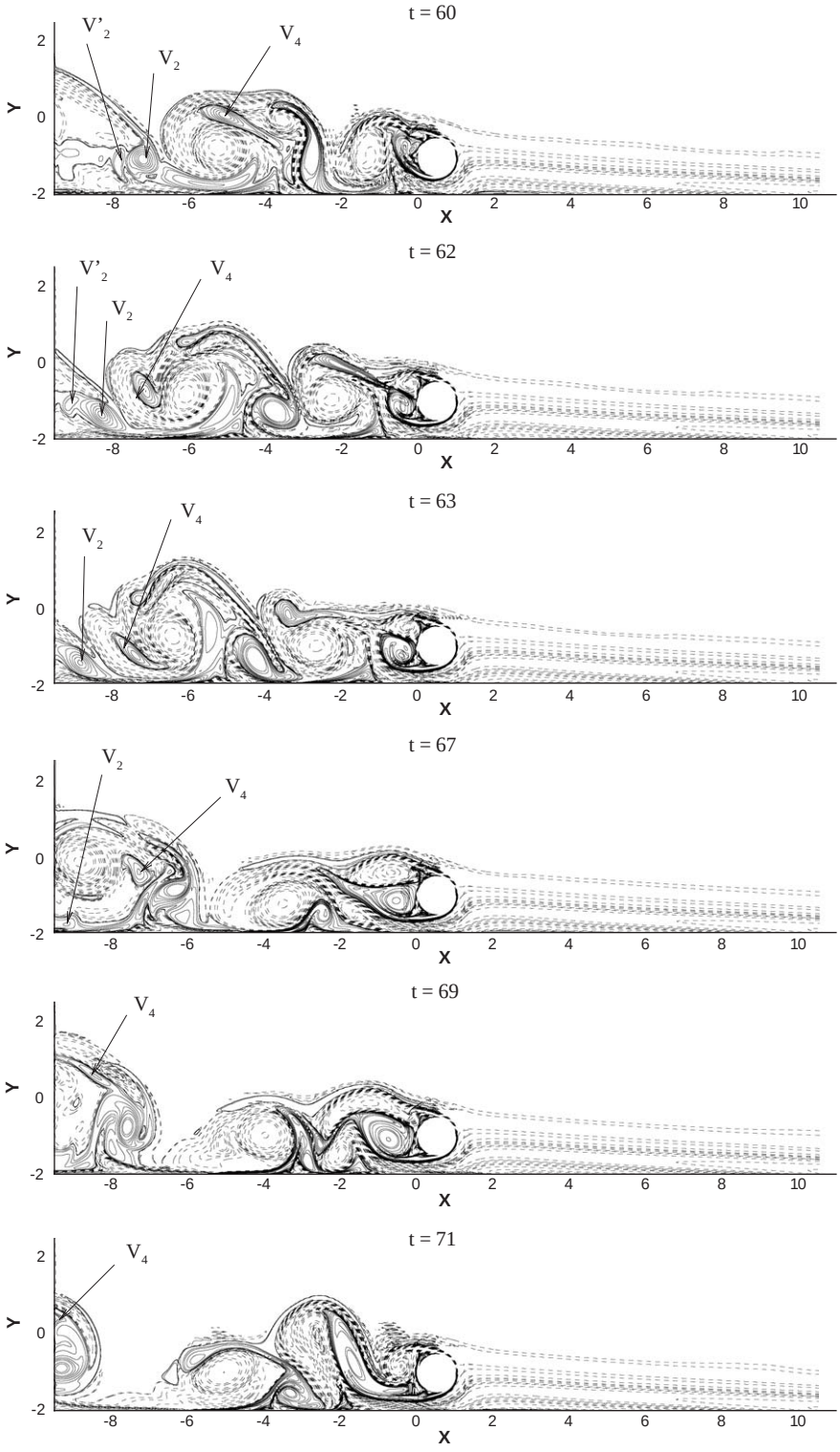

Fig. 5. (*Continued*)

4.2. Instability mechanism

The vorticity dynamics discussed for this problem in the previous section shows that this flow is highly unsteady and dominated by the vortex-induced instability that was discussed in Sengupta et al. (2003a) and the references contained therein. However, the problems of vortex-induced instability in Sengupta et al. (2003a, c) are easier,

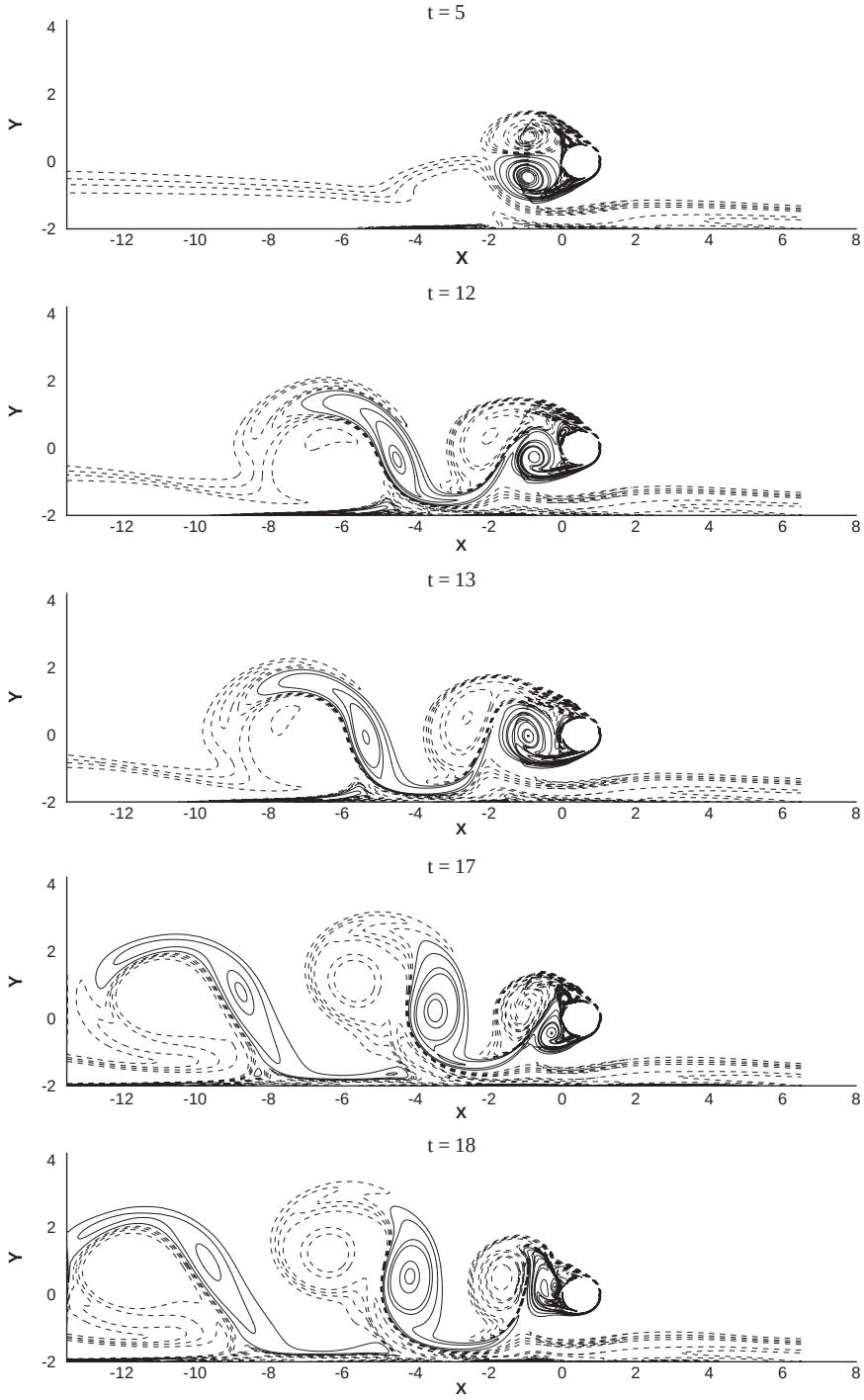

Fig. 6. Vorticity contours at indicated times for $G/D = 1.5$. The dashed lines are the negative vorticity contours.

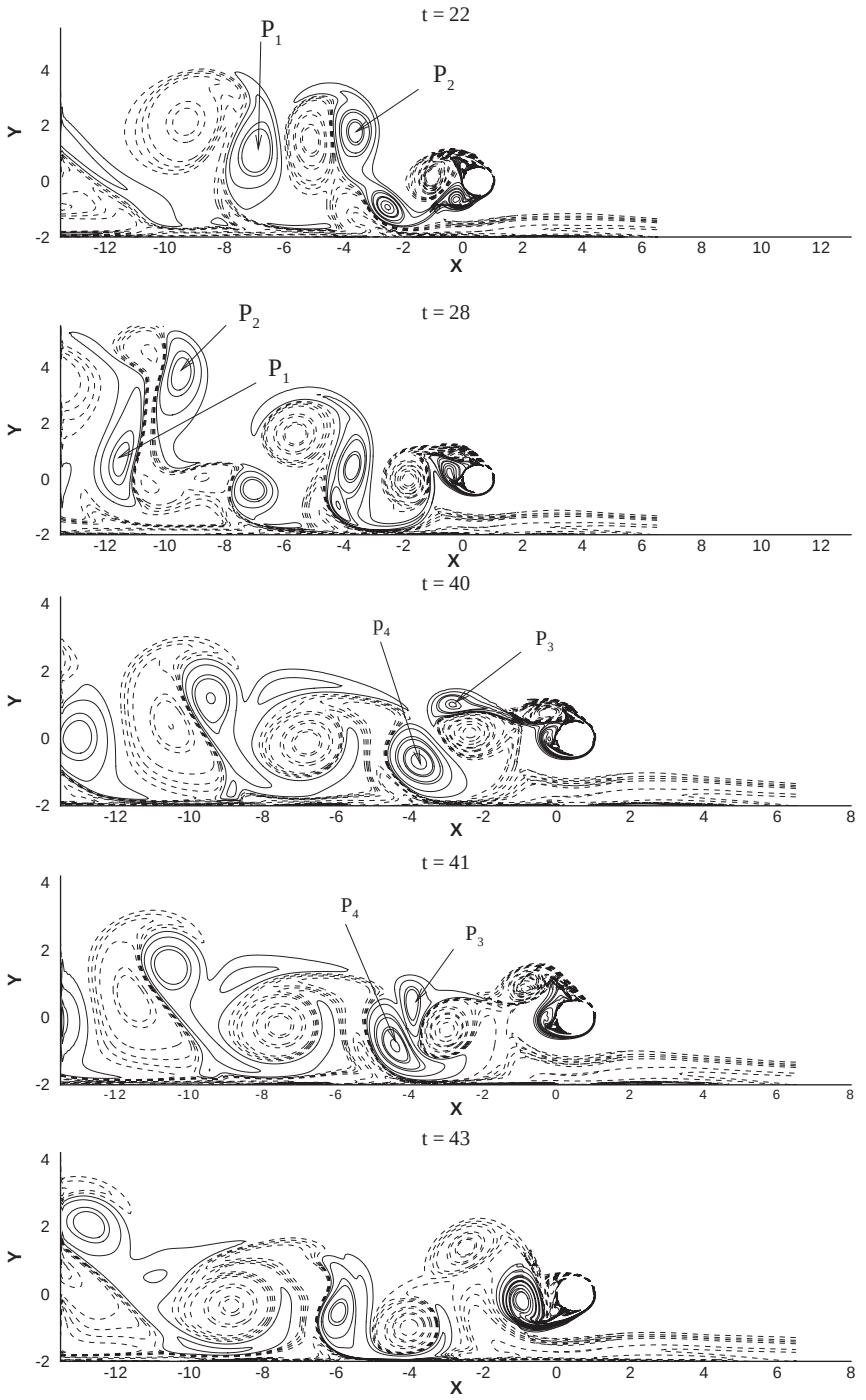

Fig. 6. (*Continued*)

in the sense that the instability originates from an equilibrium state that is steady. The results presented in this work show that this is truly an unsteady flow and its instability study requires modification of the method used in Sengupta et al. (2003a, c). The basic equations remain the same; it is only the way the instability of the unsteady flow is triggered that has to be interpreted properly. We are looking at how a dynamical system moves from one equilibrium state to another due to the presence of rapidly varying disturbance field. It is also equally relevant to point

out that the theory is not the usual small disturbance theory, as one can account for large disturbances to discuss nonlinear instability as well.

Thus, in the present paper we take the presence of the plane wall as a source of perturbation for the flow past the cylinder and *vice versa*. During such an interaction, we notice large spatio-temporal growth of the disturbance field. Unlike turbulent flows, where the time scales of the primary and the disturbance flow fields are widely separated, here the time scales are superposed. Hence, a customary Reynolds averaging will not be very appropriate. It is for the same reason that Reynolds-averaged Navier–Stokes equations do not produce satisfactory results for massively separated flows, as is the case considered here. In the following, the brief outline of the instability analysis is restated for the sake of completeness. For the incompressible flow studied here, the redistribution of the total mechanical energy can be obtained, if one identifies the total pressure as a measure of total mechanical energy ($E = p/\rho + \frac{1}{2}V^2$) of the dynamical system. The governing equation for this energy is obtained by taking divergence of the rotational form of the Navier–Stokes equation and is given by

$$\nabla^2 E = \omega^2 - \mathbf{V}\cdot\boldsymbol{\nabla} \times \boldsymbol{\omega}. \tag{4.1}$$

If one divides E into an equilibrium or reference state and a disturbance part by $E = E_m + E_d$, and substitutes in Eq. (4.1), the disturbance energy equation is given by

$$\nabla^2 E_d = 2\boldsymbol{\omega}_m\cdot\boldsymbol{\omega}_d + \boldsymbol{\omega}_d\cdot\boldsymbol{\omega}_d - V_m\cdot\boldsymbol{\nabla} \times \boldsymbol{\omega}_d - \mathbf{V}_d\cdot\boldsymbol{\nabla} \times \boldsymbol{\omega}_m - \mathbf{V}_d\cdot\boldsymbol{\nabla} \times \boldsymbol{\omega}_d. \tag{4.2}$$

In this equation $\mathbf{V}$ and $\boldsymbol{\omega}$ represent velocity and vorticity fields, respectively. The subscripts m and d refer to mean and disturbance quantities. It is possible to study the evolution of disturbance energy without solving Eq. (4.2) at different time instants, if some well-known properties of Poisson equation are invoked.

The last three terms of Eq. (4.2) are kinematic terms and not the dissipation—although they are proportional. While the dissipation is always a drain of energy, these kinematic terms can have influence on the disturbance energy, either as source or sink, depending on the orientation of velocity vector with respect to the $\nabla^2\mathbf{V}$ vector. If one invokes the analogy of heat transfer [see Sommerfeld (1949, pp. 33–35)] with mechanical energy transfer via Eq. (4.2), then a negative right-hand side is equivalent to a heat source. The gradient of energy, ∇E can be interpreted as signifying the magnitude and direction of energy flow. Hence, a divergence of the gradient term, operating on the energy, represents the outflow of energy, per unit time, per unit volume emanating from the surface of the control volume surrounding any point in the flow field. A negative right-hand side of Eq. (4.2) therefore implies a source, and a positive quantity will indicate a sink of disturbance energy. The simultaneous presence of a disturbance energy *source* and *sink* establishes a secondary flow that could be either steady or unsteady, depending on the time variation of disturbance energy.

This generic mechanism of instability is based on the full Navier–Stokes equation without any simplifying assumptions. Also, one notes that the above equation can be used to study both the linear and the nonlinear mechanism in studying the evolution of disturbance energy.

Unlike in the studies of Sengupta et al. (2003a, c), where there existed a steady mean field, here one cannot identify a steady mean field. To obviate this difficulty, we introduce the concept of instantaneous instability, where we would use Eq. (4.2) with the mean field and disturbance field defined by instantaneous values of the physical variables. Thus the mean field of any variable f, at a time instant t, is identified as $f_m = f(t)$, so that the disturbance field is given by $f_d = f(t + dt) - f(t)$, where dt is the increment of time in the study.

In Fig. 7, the right-hand side of Eq. (4.2) is shown plotted for different t. In Ω_1 the disturbance energy variation is lower as compared to that in Ω_2 (the subdomains as defined in Fig. 1). This is due to velocity-vorticity interaction terms when the streamlines are strongly curved. This was also noted in Sengupta et al. (2003c) for flow past a rotating circular cylinder. In Fig. 7, only selected lower values of contours in the range of -2 to $+2$ are plotted, with the negative contours shown as dashed lines. Higher-magnitude contours are located close to the cylinder surface within the plotted contours. The instability phenomenon is indicated at those time instants for which the streamline contours have been shown in Fig. 3. It is clearly evident that the site of disturbance energy growth and decay occurs where the vortices are located. At early times, such as at $t = 8$, one notices that the disturbance energy *source* is located where the positive vortex is located in Fig. 5. Also, at early times, the disturbance energy is associated with the vortical activities of the cylinder. However, at later times, during $t = 66-71$, disturbance energy *sources* are also present near the plane wall that is caused by the vortex-induced instability—of the kind reported in Sengupta et al. (2003a–c). The lift increase during $t = 69-73$ is associated with growth of disturbance energy, as shown in the figure.

For the larger gap ratio ($G/D = 1.5$) case, the disturbance energy evolution is shown in Fig. 8, during the time interval $t = 60-82$. The negative and positive contours are seen in pairs in the near-wake. Once again, the

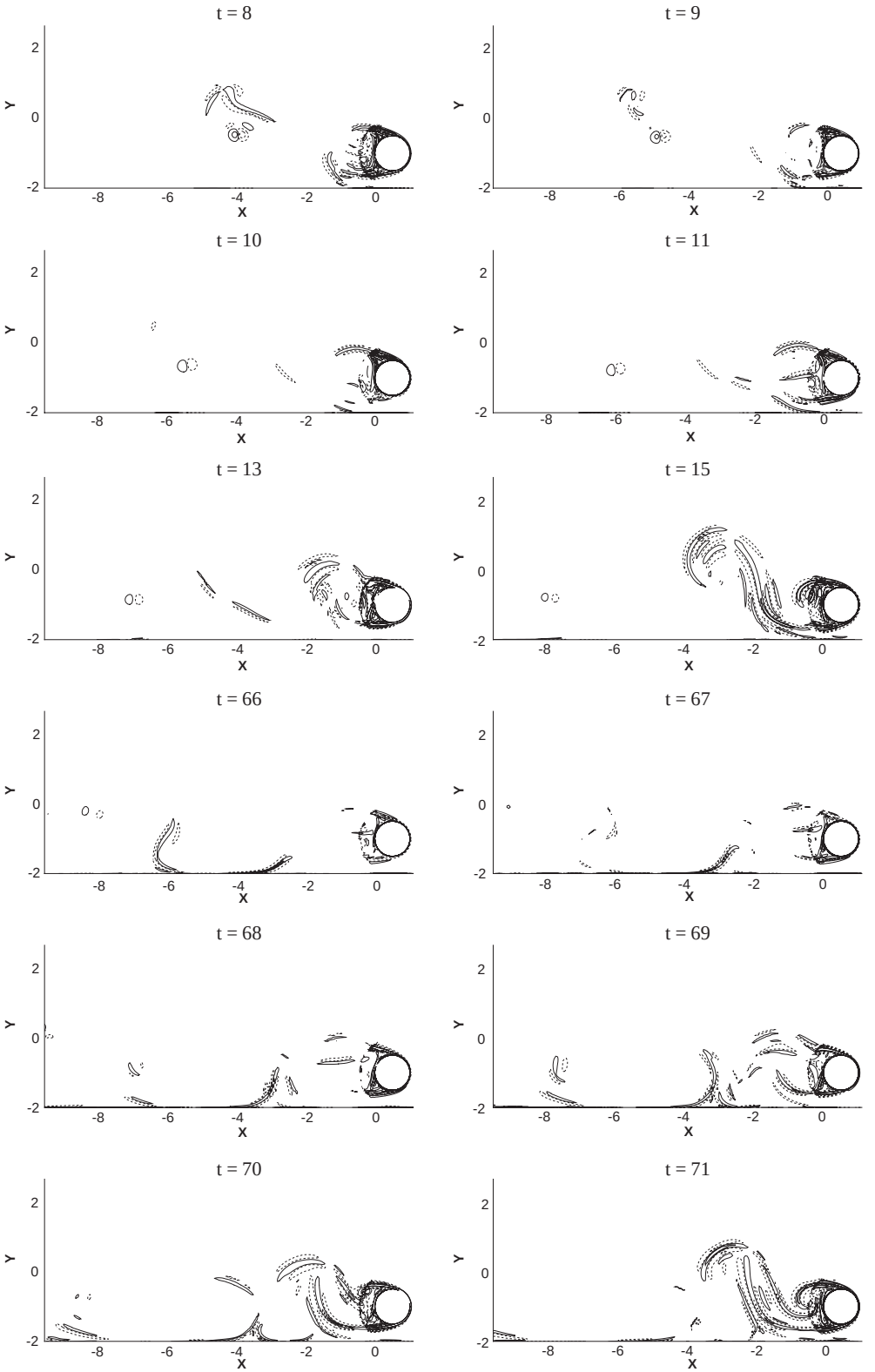

Fig. 7. The right-hand side of the disturbance energy equation (Eq. (4.2)) for $G/D = 0.5$. The negative contours (source term) are shown as dashed lines.

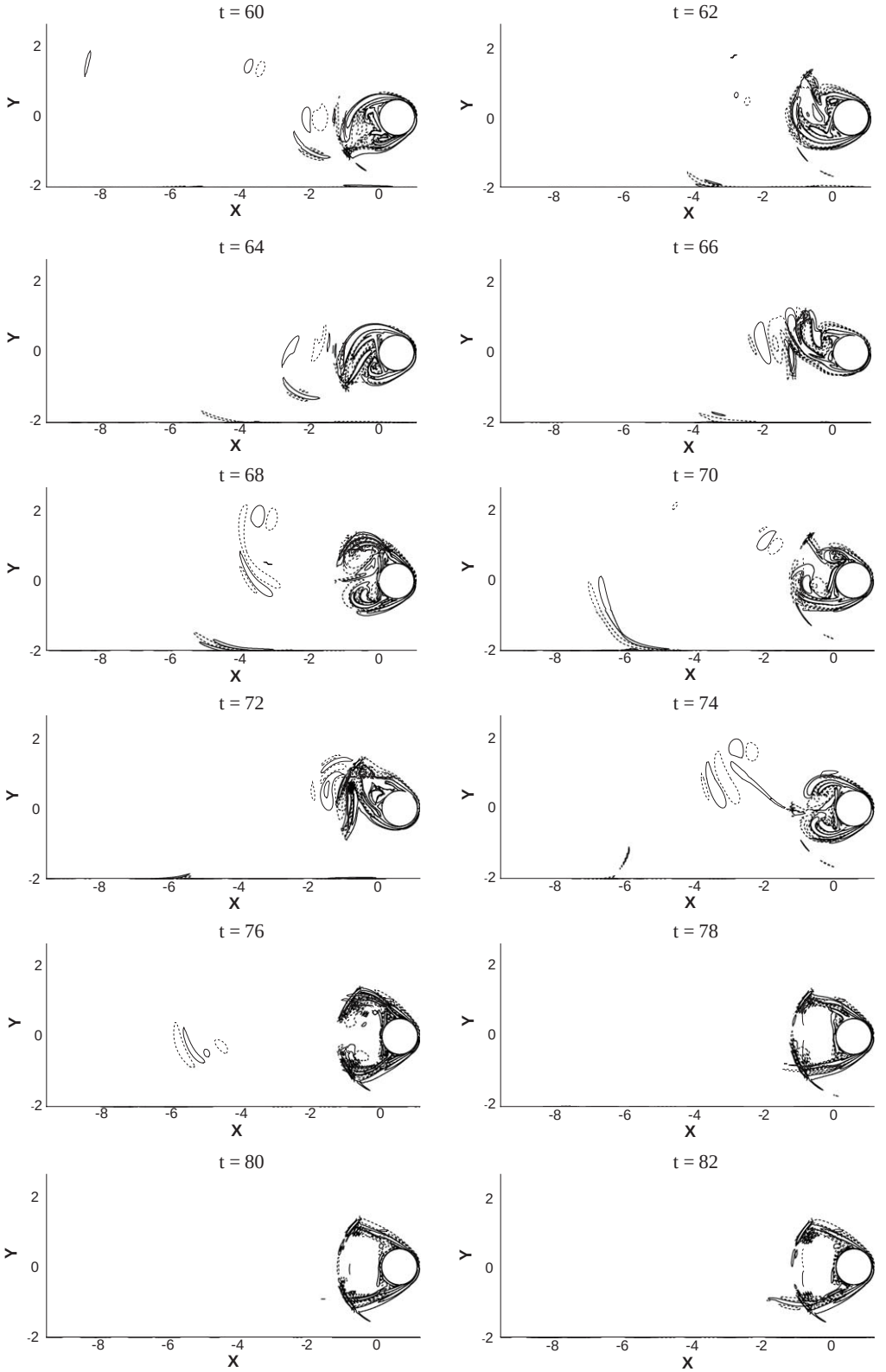

Fig. 8. The right-hand side of the disturbance energy equation (Eq. (4.2)) for $G/D = 1.5$. The negative contours (source term) are shown as dashed lines.

major vortex-induced instability is seen to occur near the cylinder surface, with very little instability on the plane wall shear layer.

5. Summary

In this study of a circular cylinder near to a solid wall, the load is computed for two different gap ratio cases. The lift and drag coefficients obtained and the observed flow behaviour match well with experimental results. The effect of the plane wall on flow around the cylinder can easily be understood with the help of vorticity dynamics and the vortex-induced instability theory of Sengupta et al. (2003a). It is clearly seen that such an interaction is a strong function of the gap between the cylinder and the plane wall. For the smaller gap ratio case, the interaction between the two vorticity field is significant and the flow over the flat plate suffers unsteady separation ahead and behind the cylinder. Such interactions begin because of the impressed adverse pressure gradient. As the adverse pressure gradient, upstream of the cylinder, weakens with increasing the gap ratio, for the higher gap ratio case the flow separation upstream of the cylinder is negligibly weak. Also, for the lower gap ratio case, the cylinder is exposed to an oncoming shear flow, that has a tendency to weaken the shed vorticity from the lower half of the cylinder. However, the vortex-induced instability strengthens this vorticity in the wake. For this case, one sees an additional positive vorticity patch developing on the shoulder of the cylinder. This is not seen for the higher gap ratio case.

It is also seen that the flow is inherently unsteady and for such flows one can talk of instability of an unsteady flow, by reinterpreting the receptivity theory proposed in Sengupta et al. (2003a, c). The instantaneous instability picture shown in Figs. 7 and 8, also shows that the instability is mainly determined by the gap and originates from the surface of the cylinder, and not from the plane surface.

References

Bearman, P.W., Zdravkovich, M.M., 1978. Flow around a circular cylinder near a plane boundary. Journal of Fluid Mechanics 89, 33–47.

Kiya, M., Tamura, M., Arie, M., 1980. Vortex shedding from a circular cylinder in moderate-Reynolds-number shear flow. Journal of Fluid Mechanics 141, 721–735.

Lei, C., Cheng, L., Kavanagh, K., 1999. Re-examination of the effect of a plane boundary on force and vortex shedding of a circular cylinder. Journal of Wind Engineering 80, 263–286.

Lim, T.T., Sengupta, T.K., Chattopadhyay, M., 2004. A visual study of vortex-induced subcritical instability on a flat plate laminar boundary layer. Experiments in Fluids 37, 47–55.

Nair, M.T., Sengupta, T.K., Chauhan, U.S., 1998. Flow past rotating cylinders at high Reynolds numbers using higher order upwind scheme. Computers and Fluids 27, 47–70.

Price, S.J., Sumner, D., Smith, J.G., Leong, K., Paidoussis, M.P., 2002. Flow visualization around a circular cylinder near to a plane wall. Journal of Fluids and Structures 16, 175–191.

Robertson, J.M., 1969. Hydrodynamics in Theory and Application. Dover, New York.

Sengupta, T.K., 2004. Fundamentals of Computational Fluid Dynamics. Universities Press, Hyderabad, India.

Sengupta, T.K., De, S., Sarkar, S., 2003a. Vortex-induced instability of incompressible wall-bounded shear layer. Journal of Fluid Mechanics 493, 277–286.

Sengupta, T.K., Ganeriwal, G., De, S., 2003b. Analysis of central and upwind compact schemes. Journal of Computational Physics 192, 677–694.

Sengupta, T.K., Kasliwal, A., De, S., Nair, M., 2003c. Temporal flow instability for Magnus–Robins effect at high rotation rates. Journal of Fluids and Structures 17, 941–953.

Sengupta, T.K., Guntaka, A., Dey, S., 2004. Navier–Stokes solution by new compact scheme for incompressible flows. Journal of Scientific Computing 21, 269–282.

Sommerfeld, A., 1949. Partial Differential Equation in Physics. Academic Press, New York, USA.

Tuncer, I.H., 1997. Two dimensional unsteady Navier–Stokes solution method with moving overset grids. AIAA Journal 35, 471–476.

Van Der Vorst, H.A., 1992. BI-CGSTAB: a fast and smoothly converging variant of BI-CG for the solution of non-symmetric linear systems. SIAM Journal of Scientific and Statistical Computing 13, 631–644.

Zdravkovich, M.M., 1985. Forces on a circular cylinder near a plane wall. Applied Ocean Research 7, 197–201.

Zdravkovich, M.M., 1997. Flow Around Circular Cylinders, vol. 1: Fundamentals. Oxford University Press, Oxford, UK.

Further reading

Taneda, S., 1965. Experimental investigation of vortex streets. Journal of the Physical Society of Japan 20, 1714–1721.